ACS APPLIED ENERGY MATERIALS

www.acsaem.org Article

Raman Scattering Methods for Monitoring the Electric Properties of the Postannealed Bulk Heterojunction

Daxin Zhang, Shuo Yang, Wenshi Zhao, Lili Yang, Yang Liu, Maobin Wei, Lei Chen,* and Jinghai Yang*

Cite This: *ACS Appl. Energy Mater.* 2021, 4, 8360–8367 Read Online

ACCESS | Metrics & More | Article Recommendations | SI Supporting Information

ABSTRACT: In the case of bulk heterojunctions (BHJs) of regioregular poly(3-hexylthiophene) (P3HT) and the soluble fullerene derivative [6,6]-phenyl-C_{61}-butyric acid methyl ester (PCBM), electrical properties have been studied based on the Raman spectroscopy. Significantly, a well enough noteworthy phenomenon is the ″return-back″ shift of the Raman signal at the ~1450 cm^{-1} with increasing annealing temperature, which was first observed using the normal Raman spectroscopy of the BHJ system. Based on the Herzberg−Teller coupling term in the organic−organic system, the ″return-back″ shift may be due to the charge transfer (CT), resulting in the significant change of resistivity (ρ). More importantly, the low annealing temperature-dependent frequency shift (ν) is carefully investigated with ρ, and $\rho \propto (-\nu)^2$. In addition, the connection between Raman intensity and ρ is also established. This study is unprecedented to establish a clear connection between frequency shift and electrical properties, indicating that the Raman technique opens an avenue to analyze the electrical properties and characterize the performance of the battery.

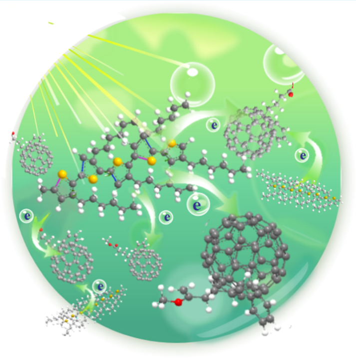

KEYWORDS: *Raman spectroscopy, Hall element, electrical properties, bulk heterojunction (BHJ), Herzberg−Teller coupling term*

■ INTRODUCTION

Polymer solar cell (PSC) system has attracted considerable interest due to simple/fast roll-to-roll production and its potential for low cost, lightweight, and flexibility since their discovery in 1985.[1−4] Through the efforts of several generations of scientists, the power conversion efficiency (PCE) of polymer batteries has now broken through the 10% mark and is moving toward materialization.[5] The highest PCE of polymer photovoltaic systems has been reported for devices utilizing the conjugated polymer/fullerene bulk heterojunction (BHJ), which consists of blended electron-donating (donor) and electron-accepting (acceptor) materials.[6] It is worth investigating that the most classic BHJ system exploiting the properties of the soluble fullerene derivative consists of poly(3-hexylthiophene) (P3HT) as the electron donor and [6,6]-phenyl-C_{61}-butyric acid methyl ester (PCBM) as the electron receptor.[7,8] There is great experimental interest in P3HT:PCBM because theoretical studies have achieved high quantum efficiencies, facilitated by the presence of a quasi-bicontinuous, interpenetrating network of electron donors and acceptors.[9,10] However, compared with inorganic batteries, the PCE still needs to be improved, mainly due to the slow charge transfer (CT) between organic molecules.

Up to now, an enormous amount of publications has been devoted to the different aspects of properties of the P3HT:PCBM blends as a model system, particularly the improvement of efficiency and mechanism analysis, towards their photovoltaic applications. Different materials, preparation methods, morphology of active layer, and other factors have different effects on preparation efficiency. The reported thermal-treatment dependence of the PCE of such binaries suggests that phase behavior and the resulting microstructure play a dominant role in the performance of devices.[11] From references, the annealing treatment facilitates the crystallinity of the P3HT:PCBM blends via demixing of PCBM and stacking of P3HT, which is demonstrated by the X-ray diffraction (XRD) technique or transmission electron microscopy (TEM).[12−14] However, the conclusion is all based on experiments, and few theories prove the effect of annealing treatment on the BHJ.

Raman signals could be clearly amplified by means of technology,[15−17] with undamaged and ultrasensitive characteristics and widely applied in chemical analysis, material science, and biomedicine.[18−21] A large number of papers have studied the CT mechanism using Raman scattering technology, which extends from inorganic substrate to organic conjugate material substrate.[22−24] Raman spectroscopy has high frequently used, high resolution, and high repeatability, especially suitable for the study of CT.[25] In the system of dye-sensitized solar cells (DSSCs), the ZnO−TiO_2 composite semiconductor transport layer was also utilized as a SERS substrate to study the

Received: June 3, 2021
Accepted: July 30, 2021
Published: August 11, 2021

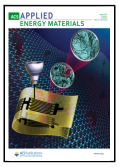

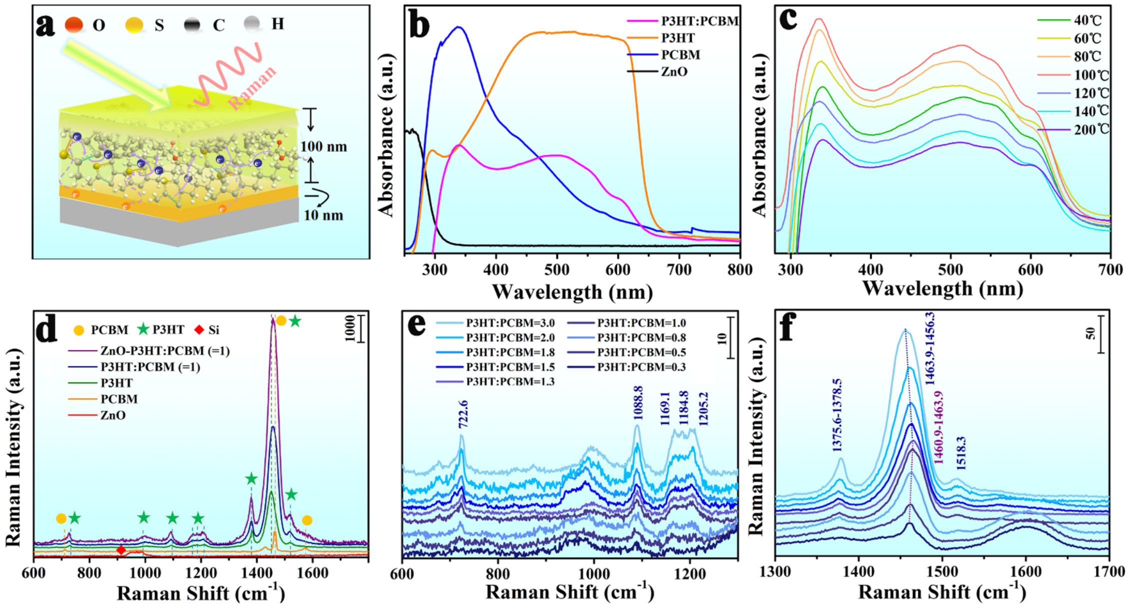

Figure 1. (a) Schematic diagram of the ZnO/P3HT:PCBM BHJ thin films. Orange represents the ZnO thin film obtained by magnetron sputtering with a thickness of about 10 nm and yellowish-green represents the P3HT:PCBM thin film obtained by the spin-coating method with a thickness of about 100 nm. (b) UV−vis absorption spectra of the ZnO thin film (black line), pure P3HT (red line), pure PCBM (blue line), and P3HT:PCBM (weight to weight = 1, pink line). (c) UV−vis absorption spectra of the P3HT:PCBM thin film (weight to weight = 1) after different annealing temperatures of 100 °C (red line), 80 °C (orange line), 60 °C (yellow line), 40 °C (green line), 120 °C (blue line), 140 °C (cyan line), and 200 °C (purple line). (d) Normalized Raman spectra of ZnO (red line), pure P3HT (green line), pure PCBM (yellow line), P3HT:PCBM (weight to weight = 1, blue line), and ZnO/P3HT:PCBM (weight to weight = 1, purple line). The dash-dotted lines are Raman modes of the pure P3HT and PCBM. (e, f) Normalized Raman spectra of P3HT:PCBM (0.3−3.0 mL). Here, the concentrations of P3HT and PCBM are 10^{-4} and 10^{-2} M, respectively.

contribution of electromagnetic fields to CT. Moreover, the crystallization hindrance of PCBM to P3HT was demonstrated using the area comparison of Raman vibration peaks, which requires annealing treatment.[26] It is particularly necessary to analyze the HBJ at different annealing temperatures by Raman spectroscopy, especially the light response.

Here, the system of ZnO as the electron transport layer and P3HT:PCBM as the BHJ was established, and both Raman spectra were affected by electrical properties changed clearly in the BHJ system with different annealing temperatures. A ″return-back″ shift occurs in the Raman spectra of the P3HT:PCBM and ZnO/P3HT:PCBM systems. Through the Herzberg−Teller coupling term and Hall element, the intensity and the frequency of Raman signal are influenced by electrical properties such as resistivity (ρ). Interestingly, the experimental relationship between ρ and Raman displacement (ν) in Raman spectra was first discovered. Moreover, Raman strength also has a corresponding relationship with the ρ. In the ZnO/P3HT:PCBM system, the relationship between ρ and ν is equally appropriate, whereas Raman intensity is enhanced compared with that of the BHJ system due to the resonance coupling of ZnO. This study indicates that Raman spectroscopy can be used as a method of monitoring electrical properties, which lays the foundation of the electrical properties characterization of the BHJ.

2. RESULTS AND DISCUSSION

The surface of the BHJ is smooth at the annealing temperatures above 100 °C (Figures S2 and S3), and the addition of PCBM breaks up the π-stacked lamellar chains in the P3HT system, resulting in low crystallinity reduction (Figure S4). Heat treatment is one of the primary means to adjust crystallinity, leading to the better optical response of thin films. The obtained UV−vis absorption spectra are given in Figure 1b. The ZnO thin film obtained by magnetron sputtering presented an absorption peak in the deep UV region, requiring greater energy to make it undergo a transition, which indicated that the ZnO molecular transition cannot be excited by 514 nm laser excitation. The dominant absorption of PCBM is at ∼335 nm in the near-UV region due to the ${}^1T_{1u}$−${}^1A_g$ electron transitions in C_{60}, and its tail extended to the near-infrared region due to lighting scatting or other experimental artifacts.[27] The absorption peak of P3HT is in the near-infrared region, which are ∼600, 550, and 515 nm, respectively.[26,27] The low-energy absorption band is due to the transition between the regioregular P3HT interbond states. The two higher ones are the 0−0 and 0−1 transitions in the in-bond state. Both transitions are in the visible region, leading to the presence of SPR enhancement and a stronger signal with a 514 nm laser excitation. Higher-energy transitions at about 300 nm are the $\pi \rightarrow \pi^*$ electron−phonon interaction connected with the aromatic ring stretching mode. The blend system is obviously expressed as the simple superposition of two materials, which means there is no effect. However, the most important difference between the P3HT and BHJ is the disappearance of vibronic progression of the absorption band of P3HT because the addition of PCBM interrupted the crystalline growth of P3HT.[28] A disruption of the formation of P3HT crystallites simultaneously causes a significant decrease in its intensity.

The UV−vis absorption spectra of P3HT:PCBM (weight to weight = 1) after different annealing temperatures are shown in Figure 1c. In the range of 40−100 °C, the absorption capacity of light increases and the absorption peak at about 340 nm shows a slight blue-shift with the increase of annealing temperature. However, when the annealing temperature exceeds 100 °C, the absorption peak is red-shifted weakly, and the absorption intensity decreased. For semiconductor materials, the surface plasma frequency ω_p depends on[29−33]

$$\omega_{\mathrm{p}} = \left(\frac{4\pi Ne^2}{\varepsilon_\infty m_{\mathrm{e}}}\right)^{1/2} = \frac{C}{\lambda} \tag{1}$$

Here, ε is the dielectric constant and is related to the properties of the matter itself. M_e is effective electron mass and basic constant. N is the carrier concentration and e is the electron charge constant. Here, surface plasmon resonance (SPR) is mainly monitored by N obtained by the Hall element in Table 1. In Table 1, N first increases and then decreases with the increase in the annealing temperature. In the range of 40−100 °C, N increases, leading to a blue-shift with an increase in the annealing temperature. In addition, a red-shift is due to the decrease in N.

Table 1. Hall Element's Test Data for the Samples after Different Annealing Temperatures, as well as Pure P3HT and PCBM[a]

annealing temperature (°C)	resistivity (Ω·cm × 10^3)	carrier density (×10^{13})	Hall coefficient (R_H × 10^6)
40	1.1686	1.2040	3.8112
60	0.9269	9.2043	2.9023
80	0.8780	12.942	2.3222
100	0.8492	47.473	0.6613
120	1.0645	12.042	0.7109
140	1.1425	3.3578	0.7736
200	1.6391	0.5906	2.0140
P3HT	1.3705	2.4667	1.3143
PCBM	1.1230	4.6959	2.0695

[a] Here, the samples are P3HT:PCBM (weight to weight = 1).

Raman spectroscopy is a powerful and promising method for exploring molecular structures, especially for systems with varying annealing temperatures. Normalized Raman spectra of the system obtained with a 514 nm excitation are shown in Figure 1d, which were ZnO (red line), P3HT (green line), PCBM (yellow line), P3HT:PCBM (weight to weight = 1, blue line), and ZnO/P3HT:PCBM (weight to weight = 1, purple line) respectively. The frequency shifts and assignments of the bands are listed in Table 2. Because the excitation energy is too low to excite electrons of ZnO, the observed Raman signal is assigned to Si. Also, four weak vibration peaks at 1425, 1462, 1575, and 700 cm^{-1}, respectively, are assigned to the C_{60} of PCBM.[26] Because of the SPR effect, P3HT has a relatively strong Raman signal. The assignments of the Raman peaks are shown in Table 2. Thereinto, the peak at ~873 cm^{-1} attributed to the C−H out-of-plane deformation was not observed because Raman vibration peaks are too weak and drowned in noise. According to Figure 1d, the signals of the BHJ are mostly similar to those of the P3HT, whereas there is a certain deviation in the frequency shift. The red-shift of the Raman peaks at ~727, 1090, and 1380 cm^{-1} was due to the high electron mobility of the receptor PCBM. However, the signal located at 1450−1460 cm^{-1} is a mixture of P3HT and PCBM without bonding.[35−37] PCBM located at 1575 cm^{-1} is overlaid by the peak assigned to P3HT. When the BHJ grew on the ZnO surface, Raman intensities of peaks at 727, 1090, and 1380 cm^{-1} are enhanced due to the effect of electromagnetic fields, and the increase of electron mobility makes the frequency of Raman peaks to the lower wavenumber. The mixed-signal peak deviates because of electron mobility. It will be affected by the annealing temperature and doping amount, which will be analyzed in detail. The peak positions in these spectra are measured with an accuracy of ±0.1 cm^{-1}, as indicated by the line-shape analyses of different bands.

Table 2. Wavenumbers, Assignments, and Sample of the Bands at 514 nm Excitation Wavelength in the Normalized Raman Spectra of Pure P3HT and PCBM[34,35] [a]

wavenumber (cm^{-1})	band assignments	sample
727	antisymmetric ring ν (C_α-S−C_α)	P3HT
1003	ν (C_β−C_{alkyl})	P3HT
1090	γ (C−H)	P3HT
1170	symmetric ν (C_α−C_α)	P3HT
1184	ν (C_α−C_α)	P3HT
1210	ν (C_β−H)	P3HT
1380	skeletal ν (C_β−C_β)	P3HT
1425	Hg(7) of the C_{60}	PCBM
1450	symmetric ν (C_α = C_β)	P3HT
1482	G_g(6) of the C_{60}	PCBM
1515	antisymmetric ν (C_α = C_β)	P3HT
1575	H_g(8) of the C_{60}	PCBM

[a] ν, stretching and γ, bending. For ring vibrations, the corresponding vibrational modes of benzene and the symmetry species under C_{2v} symmetry are indicated.

According to the normalized Raman spectra of P3HT:PCBM (0.3−3.0 mL) in Figure 1e,f, the overall Raman peaks of the BHJ are similar to those of P3HT, and most of the Raman peaks have no significant displacement, except peak located at ~1450 and 1375 cm^{-1}. The peak at ~1450 cm^{-1} assigned to the PCBM and P3HT originated from a combination of the C_α = C_β symmetric stretch mode and C_{60}, and the peak located at ~1375 cm^{-1} is assigned to the C_β−C_β skeletal stretch mode. The peak at ~1375 cm^{-1} shifts to the higher frequency after the addition of PCBM, which may result from the additional $\pi \rightarrow \pi^*$ conjugated interactions between C_{60}. On the other hand, the peak at ~1450 cm^{-1} changes to high frequency due to an increase in C_{60}, and then the vibration mode is inclined to simple P3HT, with an increase in P3HT. Meanwhile, the overall carrier concentration (n) decreases because the donor first balances the receptor, and then n increases when the donor is more than the receptor. Here, the shift of Raman peak is mainly due to the dominant n.[38,39] Figure 2a,b shows the normalized Raman spectra of P3HT:PCBM (weight to weight = 1) at different annealing temperatures, which were obtained with a 514 nm excitation. Also, normalized Raman intensity and shift of P3HT:PCBM (weight to weight = 1) after different annealing temperatures are shown in Table S1. Most of the Raman peaks have no obvious displacement in Figure 2a,b, except the peak located at ~1450 cm^{-1}. The peak at ~1450 cm^{-1}, which is assigned to PCBM and P3HT, originated from a combination of the C_α = C_β symmetric stretch mode and C_{60}. Surprisingly, the peak at ~1450 cm^{-1} first shifts to the high frequency and then to the low frequency. This is a phenomenon worth investigating, we consider the influence of electrical properties. Figure 2c is the relationship curve between ν and T, whereas Figure 2d is the relationship curve between Raman intensity and T. In Figure 2c, ν and T obey $\nu \approx 1412.17 \times T^{0.0068}$ at low annealing

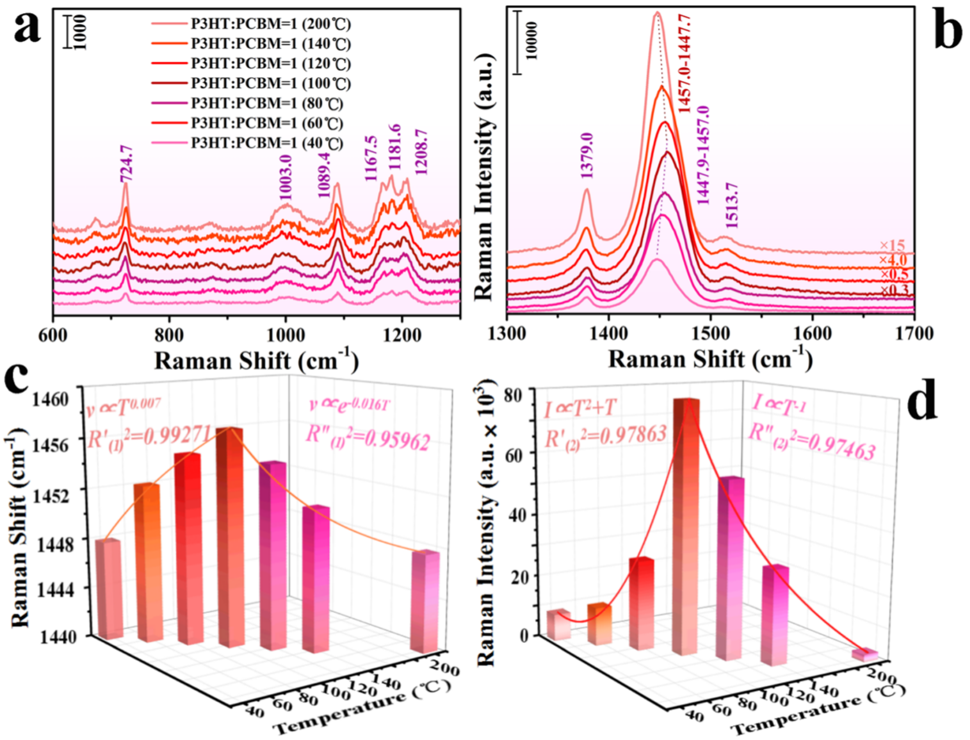

Figure 2. (a, b) Normalized Raman spectra of P3HT:PCBM (weight to weight = 1) after different annealing temperatures, which are 40, 60, 80, 100, 120, 140, and 200 °C, respectively. (c) Three-dimensional histogram of frequency shift at ∼1450 cm^{-1} and annealing temperature in the P3HT:PCBM system, and the curve is the frequency shift and annealing temperature fitting curve. (d) Three-dimensional histogram of Raman signal peak intensity at ∼1450 cm^{-1} and annealing temperature in the P3HT:PCBM system, and the curve is Raman signal peak intensity and annealing temperature fitting curve.

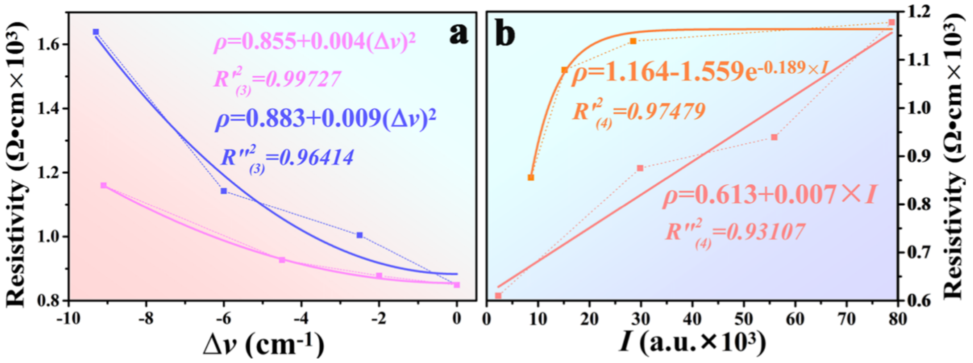

Figure 3. (a) Fitting curves of frequency shift ($\Delta\nu$) and resistivity (ρ). (Pink represents the curve after low annealing temperatures, and purple represents the curve after high annealing temperatures.) (b) Fitting curves of Raman intensity (I) and resistivity (ρ). (Orange represents the curve after low annealing temperatures, and salmon represents the curve after high annealing temperatures.)

temperature and $R'_{(1)}{}^2 = 0.99271$. At high annealing temperatures, $\nu \approx 59.97 \times e^{-0.0016T} + 1445.22$ and $R''_{(1)}{}^2 = 0.95962$. $R''_{(1)}{}^2$ is lower than $R'_{(1)}{}^2$ due to the destruction of the sample crystallization by high-temperature annealing. Frequency shift at ∼1450 cm^{-1} considered the influence of electrical properties. Hall elements get ρ after different annealing temperatures of the BHJ films in Table 1, and the temperature dependence of ρ is shown in Figure S7. In the lower temperature, the decrease of ρ is mainly determined by the CT. However, with the increase in temperature, lattice scattering (the interaction of electrons with a lattice) diminishes the CT, leading to the increase of ρ. Then, the frequency shift at ∼1450 cm^{-1} is combined with the Hall data to analyze the correlation between $\Delta\nu$ and ρ of the intrinsic properties of the BHJ films in Figure 3a. We consider the peak at 1457 cm^{-1} as zero, and $\Delta\nu$ is the difference between ν and 1457 cm^{-1}. The pink line is the fitting curve between 40 and 100 °C, whereas the purple line is the fitting curve over 100 °C. The relationship between $\Delta\nu$ and ρ is expressed as

$$\rho = A(-\Delta\nu)^2 + B \tag{2}$$

The ρ is proportional to the negative value of $\Delta\nu$. The regularity of the fitting curve of 40−100 °C is higher than that of high temperature, up to 99%. In other words, ρ is closely related to CT. Through analysis and comparison, the sensitivity of the donor or receptor to temperature in Figures S8 and S9, there may be three CT processes in the P3HT:PCBM system (Figure 4): (1) The electron is transferred from the HOMO level of the PCBM to the LUMO level to produce the resonance effect through the

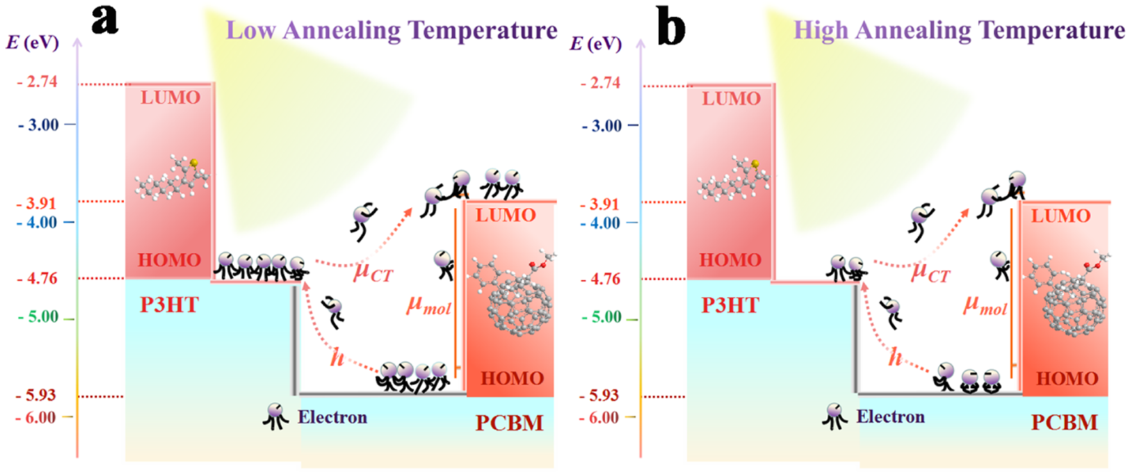

Figure 4. Energy level and electron transition diagrams for P3HT (donor) and PCBM (receptor) after low annealing temperature (a) and high annealing temperature (b), respectively.

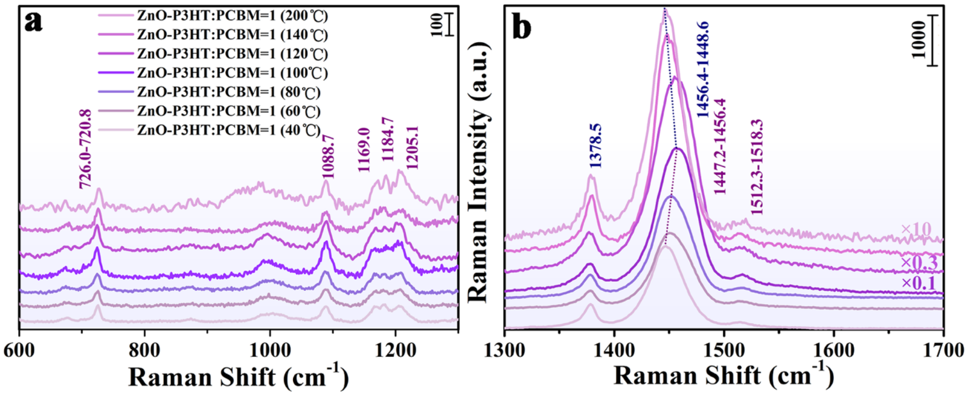

Figure 5. Normalized Raman spectra of ZnO/P3HT:PCBM (weight to weight = 1:1) after different annealing temperatures, which are 40, 60, 80, 100, 120, 140, and 200 °C.

molecular resonance (μ_{mol}). (2) The electron is transferred from the HOMO level of PCBM to the HOMO level of P3HT to realize the CT effect through the Herzberg–Teller vibronic coupling term ($h_{\text{mol-CT}}$). (3) The electron is transferred from the HOMO level of P3HT to the LUMO level of PCBM to realize the CT effect through the charge-transfer resonance (μ_{CT}). In the pure PCBM system, molecular resonance leads to $\Delta\nu$, which is about 5 cm^{-1}. Then, because of the Herzberg–Teller vibronic coupling and charge-transfer resonance accelerate electron mobility and decrease ρ, $\Delta\nu$ increases to ~10 cm^{-1} in the BHJ. In this case, the main characteristic is that $\Delta\nu$ can corroborate ρ.

Besides, ρ controlled by CT is shown in Raman intensity. Figure 2d is the relationship curve between Raman intensity and T. Raman intensity is dominant by T^2 at low temperatures, whereas Raman intensity is inversely proportional to T at high temperatures. With the increase in T, Raman intensity first increases then decreases. The intensity of a Raman transition may be obtained from the polarizability tensor ($\alpha_{\sigma\rho}$), then Albrecht rewrote $\alpha_{\sigma\rho}$ as the sum of three terms, commonly called A, B, and C, utilizing the Herzberg–Teller mixed with the vibration function.[40] In the case of the BHJ, only the C-term applies, since in the ground state, the weak coupling is involved. We, therefore, restrict our derivation to the consideration of the C-term. For simplicity, we do not consider the continuous energy levels of organic semiconductors but only the HOMO and LUMO energy levels. Here, $R(\omega)$ is converted as

$$\begin{aligned} R_{\text{mol-CT}}(\omega) &= \frac{\mu_{\text{CT}}\mu_{\text{mol}}h_{\text{mol-CT}}\langle i|Q_K|f\rangle}{[(\varepsilon_1(\omega)+2\varepsilon_0)^2+\varepsilon_2^2](\omega_{\text{CT}}^2-\omega^2+\gamma_{\text{CT}}^2)(\omega_{\text{mol}}^2-\omega^2+\gamma_{\text{mol}}^2)} \\ &= A\times B_{\text{mol-CT}}(\omega) \end{aligned} \tag{3}$$

$$A = \frac{1}{(\varepsilon_1(\omega)+2\varepsilon_0)^2+\varepsilon_2^2} \tag{4}$$

$$B_{\text{mol-CT}}(\omega) = \frac{\mu_{\text{CT}}\mu_{\text{mol}}h_{\text{mol-CT}}\langle i|Q_K|f\rangle}{(\omega_{\text{CT}}^2-\omega^2+\gamma_{\text{CT}}^2)(\omega_{\text{mol}}^2-\omega^2+\gamma_{\text{mol}}^2)} \tag{5}$$

Here, $R_{\text{mol-CT}}(\omega)$ is divided into two contributions: A and B. A is related to the dielectric constant of the potential difference between donor and acceptor and B is related to the dipole moment of electron transition. According to the Boltzmann approximation, more electrons are concentrated in each energy level of the HOMO, increasing the dipole moment and promoting the probabilistic electron transition with the increasing T. In the formula of $B_{\text{mol-CT}}(\omega)$, μ_{mol} and μ_{CT} are increased and $B(\omega)$ is increased. Here, the intensity of a Raman transition is expressed as

$$I \propto |R_{\mathrm{mol-CT}}(\omega)^2| \propto |B_{\mathrm{mol-CT}}(\omega)^2| \propto |\mu_{\mathrm{CT}}\mu_{\mathrm{mol}}|^2 \quad (6)$$

Additionally, ρ is negatively correlated with the probabilistic electron transition, so ρ is inversely proportional to μ_{mol} and μ_{CT}. Then, the Raman intensity is negatively correlated with ρ at low temperatures. However, ρ is a negative exponential function of Raman intensity in Figure 3b. Under lattice scattering, $\rho = 0.613 + 0.007 \times I$ and $R''_{(4)}{}^2 \geq 0.93$ at high temperatures. Obviously, the fitting fits better at low temperature and ρ is related to Raman intensity in a negative exponential form, which is a noteworthy phenomenon.

When the BHJ covers the transport layer of ZnO, the ZnO/P3HT:PCBM system is formed and its Raman spectra are shown in Figure 5. Compared with the Raman spectra of the BHJ, the noteworthy difference is that the Raman peak located at ~720 cm^{-1} is shifted to 726 cm^{-1}. The Raman peak located at ~720 cm^{-1} originates from the antisymmetric C_α-S-C_α bending deformation vibrations in the thiophene ring and is shifted to a lower frequency due to the resonance coupling effect of ZnO. The other frequency shifts are the same as the results of the previous BHJ films. Raman offset and electrical properties can also be applied to the system, that is, $\rho \propto (-\Delta\nu)^2$. In addition, the Raman intensity of the ZnO films coated with the BHJ films is slightly enhanced compared with that of the BHJ films, which is also due to the enhancement caused by the ZnO resonance coupling effect.

■ CONCLUSIONS

In summary, since PSCs have high sensitivity to the annealing temperature, the electrical properties of the BHJ were monitored in normalized Raman spectra. In the P3HT:PCBM system, it was observed for the first time that the superimposed band at ~1450 cm^{-1} showed a "return-back" displacement at a turning annealing temperature of 100 °C in the normalized Raman spectrum of the BHJ. Also, Raman intensity shows a similar return-back change. According to the Herzberg−Teller coupling term and Hall elements, it is an unprecedented discovery that ρ is positively correlated with the square of $\Delta\nu$. Besides, at low temperatures, ρ has a well enough negative exponential relationship with Raman intensity, whereas ρ is negatively proportional to Raman intensity at high temperatures. The correlations are also applicable to the ZnO/P3HT:PCBM systems and similar systems. Raman spectroscopy can not only be used as a new means of monitoring the electrical properties to extend the photoelectric response of the spectrum but also be increasingly applied to the characterization of battery performance.

■ ASSOCIATED CONTENT

Supporting Information

The Supporting Information is available free of charge at https://pubs.acs.org/doi/10.1021/acsaem.1c01600.

> Experimental section; SEM of P3HT, PCBM, P3HT:PCBM (weight to weight = 1) at different annealing temperatures; XRD of pure P3HT (powder), pure PCBM (powder), and the thin film of P3HT:PCBM (weight to weight = 1) at an annealing temperature of 100 °C; calculation of E_g of the ZnO and P3HT:PCBM films with no annealing and different annealing temperatures; the Raman intensity (I) and shift (ν) of the BHJ at different annealing temperatures; the differential thermal analysis diagram of P3HT (power), PCBM (power), and P3HT:PCBM (power); analysis of the relation of Hall element and annealing temperature; and normalized Raman spectra of the thin film of P3HT (2.5 mg/mL) and PCBM (2.5 mg/mL) at different annealing temperatures (PDF)

■ AUTHOR INFORMATION

Corresponding Authors

Lei Chen − *Key Laboratory of Functional Materials Physics and Chemistry of the Ministry of Education, Jilin Normal University, Changchun 130103, P. R. China;* orcid.org/0000-0003-2616-2190; Email: chenlei@jlnu.edu.cn

Jinghai Yang − *Key Laboratory of Functional Materials Physics and Chemistry of the Ministry of Education, Jilin Normal University, Changchun 130103, P. R. China;* orcid.org/0000-0001-8409-6035; Email: jhyang1@jlnu.edu.cn

Authors

Daxin Zhang − *Changchun Institute of Optics, Fine Mechanics and Physics, Chinese Academy of Sciences, Changchun 130033, P. R. China; University of Chinese Academy of Sciences, Beijing 100049, P. R. China; Key Laboratory of Functional Materials Physics and Chemistry of the Ministry of Education, Jilin Normal University, Changchun 130103, P. R. China*

Shuo Yang − *College of Science, Changchun University, Changchun 130022, P. R. China*

Wenshi Zhao − *Changchun Institute of Optics, Fine Mechanics and Physics, Chinese Academy of Sciences, Changchun 130033, P. R. China; University of Chinese Academy of Sciences, Beijing 100049, P. R. China; Key Laboratory of Functional Materials Physics and Chemistry of the Ministry of Education, Jilin Normal University, Changchun 130103, P. R. China*

Lili Yang − *Key Laboratory of Functional Materials Physics and Chemistry of the Ministry of Education, Jilin Normal University, Changchun 130103, P. R. China;* orcid.org/0000-0003-0333-1684

Yang Liu − *Key Laboratory of Functional Materials Physics and Chemistry of the Ministry of Education, Jilin Normal University, Changchun 130103, P. R. China;* orcid.org/0000-0003-1485-8764

Maobin Wei − *Key Laboratory of Functional Materials Physics and Chemistry of the Ministry of Education, Jilin Normal University, Changchun 130103, P. R. China*

Complete contact information is available at: https://pubs.acs.org/10.1021/acsaem.1c01600

Notes

The authors declare no competing financial interest.

■ ACKNOWLEDGMENTS

This work was supported by the National Natural Science Foundation of China (Grant nos. 61775081 and 22075101) and the Program for the Development of Science and Technology of Jilin province (Item nos. 20200801032GH and 20200301043RQ).

■ REFERENCES

(1) Heinz, B.; Daniel, K.; Franz, S.; Vojtech, N.; Anna, K. Mapping the density of states distribution of organic semiconductors by

employing energy resolved-electrochemical impedance spectroscopy. *Adv. Funct. Mater.* **2020**, *31*, No. 2007738.

(2) Ghazy, O.; Birger, F.; Ingo, L.; Katharina, L. Tuning the size and morphology of P3HT/PCBM composite nanoparticles: towards optimized water-processable organic solar cells. *Nanoscale* **2020**, *12*, 22798−22807.

(3) Krebs, F. C. Polymer solar cell modules prepared using roll-to-roll methods: Knife-over-edge coating, slot-die coating and screen printing. *Sol. Energy Mater. Sol. Cells* **2009**, *93*, 465−475.

(4) Martin, K.; Matthew, S. W.; Eric, D. G.; Tsuyoshi, S.; Takao, S.; Niyazi, S. S.; Siegfried, B. Ultrathin and lightweight organic solar cells with high flexibility. *Nat. Commun.* **2012**, *3*, No. 770.

(5) Wang, P.; Wu, Y. H.; Cai, B.; Ma, Q. S.; Zheng, X. J.; Zhang, W. H. Solution-processable perovskite solar cells toward commercialization: progress and challenges. *Adv. Funct. Mater.* **2018**, *29*, No. 1807661.

(6) Lee, Y.; Lee, S. H.; Kim, K.; Lee, J. W.; Han, K.-Y.; Kim, J.; Joo, J. Single nanoparticle of organic p-type and n-type hybrid materials: nanoscale phase separation and photovoltaic effect. *J. Mater. Chem.* **2012**, *22*, 2485−2490.

(7) Xiong, J.; Qi, Y. F.; Zhang, Q. Q.; Box, D.; Williams, K.; Tatum, J.; Das, P.; Pradhan, N. R.; Dai, Q. L. Enhanced moisture and water resistance in inverted perovskite solar cells by poly(3-hexylthiophene). *ACS Appl. Energy Mater.* **2021**, *4*, 1815−1823.

(8) Huang, W. C.; Chandrasekaran, N.; Prasad, S. K. K.; Gann, E.; Thomsen, L.; Kabra, D.; Hodgkiss, J. M.; Cheng, Y. B.; McNeill, C. R. Impact of fullerene mixing behavior on the microstructure, photophysics, and device performance of polymer/fullerene solar cells. *ACS Appl. Mater. Interfaces* **2016**, *8*, 29608−29618.

(9) Ouyang, J.; Chi, C. W.; Chen, F. C.; Xi, Q. F.; Yang, Y. High-conductivity poly (3,4-ethylenedioxythiophene): poly(styrene sulfonate) film and its application in polymer optoelectronic devices. *Adv. Funct. Mater.* **2005**, *15*, 203−208.

(10) Li, G.; Shrotriya, V.; Yao, Y.; Huang, J.; Yang, Y. Manipulating regioregular poly(3-hexylthiophene):[6,6]-phenyl-C61-butyric acid methyl ester blends—route towards high efficiency polymer solar cells. *J. Mater. Chem.* **2007**, *17*, 3126.

(11) Mihailetchi, V. D.; Xie, H. X.; de Boer, B.; Koster, L. J. A.; Blom, P. W. M. Charge transport and photocurrent generation in poly (3-hexylthiophene): Methanofullerene bulk-heterojunction solar cells. *Adv. Funct. Mater.* **2006**, *16*, 699−708.

(12) Yang, X.; van Duren, J. K. J.; Rispens, M. T.; Hummelen, J. C.; Janssen, R. A. J.; Michels, M. A. J.; Loos, J. Crystalline organization of a methanofullerene as used for plastic solar-cell applications. *Adv. Mater.* **2004**, *16*, 802−806.

(13) An, H.; Li, X. Y.; Smith, K. A.; Zhang, Y. P.; Verduzco, R.; Lutkenhaus, J. L. Regioregularity and molecular weight effects in redox-active poly(3-hexylthiophene)-block-poly(ethylene oxide) electrode binders. *ACS Appl. Energy Mater.* **2018**, *1*, 5919−5927.

(14) Müller, C.; Ferenczi, T. A. M.; Campoy-Quiles, M.; Frost, J. M.; Bradley, D. D. C.; Smith, P.; Stingelin-Stutzmann, N.; Nelson, J. Binary organic photovoltaic blends: A simple rationale for optimum compositions. *Adv. Mater.* **2008**, *20*, 3510−3515.

(15) Li, J. F.; Huang, Y. F.; Ding, Y.; Yang, Z. L.; Li, S. B.; Zhou, X. S.; Fan, F. R.; Zhang, W.; Zhou, Z. Y.; Wu, D. Y.; Ren, B.; Wang, Z. L.; Tian, Z. Q. Shell-isolated nanoparticle-enhanced Raman spectroscopy. *Nature* **2010**, *464*, 392−5.

(16) Pettinger, B.; Ren, B.; Picardi, G.; Schuster, R.; Ertl, G. Nanoscale probing of adsorbed species by tip-enhanced Raman spectroscopy. *Phys. Rev. Lett.* **2004**, *92*, No. 096101.

(17) Stőckle, R. M.; Suh, Y. D.; Deckert, V.; Zenobi, R. Nanoscale chemical analysis by tip-enhanced Raman spectroscopy. *Chem. Phys. Lett.* **2000**, *318*, 131−136.

(18) Zhou, J.; Zhang, J. S.; Yang, H. T.; Wang, Z.; Shi, J. A.; Zhou, W.; Jiang, N.; Xian, G. Y.; Qi, Q.; Weng, Y. X.; Shen, C. M.; Cheng, Z. H.; He, S. T. Plasmon-induced hot electron transfer in Au-ZnO heterogeneous nanorods for enhanced SERS. *Nanoscale* **2019**, *11*, 11782−11788.

(19) Managò, S.; Zito, G.; Rogato, A.; Casalino, M.; Esposito, E.; De Luca, A. C.; De Tommasi, E. Bioderived three-dimensional hierarchical nanostructures as efficient surface-enhanced raman scattering substrates for cell membrane probing. *ACS Appl. Mater. Interfaces* **2018**, *12*, 12406−12416.

(20) Fonseca Rodrigues, M. T.; Maroni, V. A.; Gosztola, D. J.; Yao, K. P. C.; Kalaga, K.; Shkrob, I. A.; Abraham, D. P. Lithium acetylide: A spectroscopic marker for lithium deposition during fast charging of li-ion cells. *ACS Appl. Energy Mater.* **2019**, *2*, 873−881.

(21) Pandey, J.; Mukherjee, S.; Rawat, D.; Athar, S.; Rana, K. S.; Mallik, R. C.; Soni, A. Raman spectroscopy study of phonon liquid electron crystal in copper deficient superionic thermoelectric $Cu_{2-x}Te$. *ACS Appl. Energy Mater.* **2020**, *3*, 2175−2181.

(22) Lombardi, J. R. Enhanced by organic surfaces. *Nat. Mater.* **2017**, *16*, 878−880.

(23) Lombardi, J. R. The theory of surface-enhanced Raman spectroscopy on organic semiconductors: J-aggregates. *Chem. Phys. Lett.* **2020**, *751*, No. 137553.

(24) Zhang, X.-Y.; Yang, S.; Yang, L. L.; Zhang, D. X.; Sun, Y. S.; Pang, Z. Y.; Yang, J. H.; Chen, L. Carrier dynamic monitoring of a pi-conjugated polymer: a surface-enhanced Raman scattering method. *Chem. Commun.* **2020**, *56*, 2779−2782.

(25) Wang, X.; Li, P.; Han, X. X.; Kitahama, Y.; Zhao, B.; Ozaki, Y. An enhanced degree of charge transfer in dye-sensitized solar cells with a ZnO-TiO_2/N3/Ag structure as revealed by surface-enhanced Raman scattering. *Nanoscale* **2017**, *9*, 15303−15313.

(26) Falke, S.; Eravuchira, P.; Materny, A.; Lienau, C. Raman spectroscopic identification of fullerene inclusions in polymer/fullerene blends. *J. Raman Spectrosc.* **2011**, *42*, 1897−1900.

(27) Leach, S.; Vervloet, M.; Desprks, A.; BrCheret, E.; Hare, J. P.; Dennis, T. J.; Kroto, H. W.; Taylor, R.; Walton, D. R. M. Electronic spectra and transitions of the fullerene C_{60}. *Chem. Phys.* **1992**, *160*, 451−466.

(28) Jarząbek, B.; Nitschke, P.; Hajduk, B.; Domanski, M.; Bednarski, H. In situ thermo-optical studies of polymer:fullerene blend films. *Polym. Test.* **2020**, *88*, No. 106573.

(29) Guo, T.-F.; Wen, T.-C.; Pakhomov, G. L.; Chin, X.-G.; Liou, S.-H.; Yeh, P.-H.; Yang, C.-H. Effects of film treatment on the performance of poly(3-hexylthiophene)/soluble fullerene-based organic solar cells. *Thin Solid Films* **2008**, *516*, 3138−3142.

(30) Zhang, D.; Yang, S.; Zhang, X.-Y.; Ma, N.; Han, B.; Zhao, W.; Chi, S.; Liu, Y.; Yang, J.; Chen, L. Damping resonance and refractive index effect on the layer-by-layer sputtering of Ag and Al_2O_3 on the polystyrene template. *Spectrochim. Acta, Part A* **2020**, *238*, No. 118430.

(31) Zhang, X.-Y.; Chen, L.; Wang, Y.; Zhang, Y.; Yang, J.; Choi, H. C.; Jung, Y. M. Design of tunable ultraviolet (UV) absorbance by controlling the Ag-Al co-sputtering deposition. *Spectrochim. Acta, Part A* **2018**, *197*, 37−42.

(32) Simonson, T. Dielectric Relaxation in Proteins: Microscopic and Macroscopic Models. *Int. J. Quantum Chem.* **1999**, *73*, 45−57.

(33) Paci, B.; Generosi, A.; Albertini, V. R.; Spyropoulos, G. D.; Stratakis, E.; Kymakis, E. Enhancement of photo/thermal stability of organic bulk heterojunction photovoltaic devices via gold nanoparticles doping of the active layer. *Nanoscale* **2012**, *4*, 7452−9.

(34) Saini, V.; Li, Z.; Bourdo, S.; Dervishi, E.; Xu, Y.; Ma, X.; Kunets, V. P.; Salamo, G. J.; Viswanathan, T.; Biris, A. R.; Saini, D.; Biris, A. S. Electrical, optical, and morphological properties of P3HT-MWNT nanocomposites prepared by in situ polymerization. *J. Phys. Chem. C* **2009**, *113*, 8023−8029.

(35) Tsoi, W. C.; James, D. T.; Kim, J. S.; Nicholson, P. G.; Murphy, C. E.; Bradley, D. D. C.; Nelson, J.; Kim, J. S. The nature of in-plane skeleton Raman modes of P3HT and their correlation to the degree of molecular order in P3HT:PCBM blend thin films. *J. Am. Chem. Soc.* **2011**, *133*, 9834−43.

(36) Yang, X.; Loos, J.; Veenstra, S. C.; Verhees, W. J. H.; Wienk, M. M.; Kroon, J. M.; Michels, M. A. J.; Janssen, R. A. J. Nanoscale morphology of high-performance polymer solar cells. *Nano Lett.* **2005**, *5*, 579−583.

(37) Candan, İ.; Özen, Y. Comparison of TiO_2 and ZnO electron selective layers on the inverted-type polymer solar cells. *Polym. Bull.* **2021**, *78*, 3117−3129.

(38) Zhang, X.-Y.; Han, D.; Ma, N.; Gao, R.; Zhu, A.; Guo, S.; Zhang, Y.; Wang, Y.; Yang, J.; Chen, L. Carrier density-dependent localized surface plasmon resonance and charge transfer observed by controllable semiconductor content. *J. Phys. Chem. Lett.* **2018**, *9*, 6047−6051.

(39) Luther, J. M.; Jain, P. K.; Ewers, T.; Alivisatos, A. P. Localized surface plasmon resonances arising from free carriers in doped quantum dots. *Nat. Mater.* **2011**, *10*, 361−366.

(40) Lombardi, J. R.; Birke, R. L. A Unified Approach to Surface-Enhanced Raman Spectroscopy. *J. Phys. Chem. C* **2008**, *112*, 5605−5617.